mathematics

MDPI

Article

Optimization of Magnetic Pump Impeller Based on Blade Load Curve and Internal Flow Study

Ruijie Zhang [1], Jiaqiong Wang [1,2,*], Wenfei Qian [1] and Linlin Geng [1]

[1] Research Center of Fluid Machinery Engineering and Technology, Jiangsu University, Zhenjiang 212013, China; zhangruijie1004@gmail.com (R.Z.); 1000003796@ujs.edu.cn (W.Q.); linlin.geng@ujs.edu.cn (L.G.)
[2] Wenling Fluid Machinery Technology Institute, Jiangsu University, Zhenjiang 212013, China
* Correspondence: wjq399@126.com

Abstract: Compared to traditional centrifugal pumps, magnetic pumps are widely used in industries such as chemical, pharmaceutical, and petroleum due to their characteristics of leakage-free operation and the ability to transport toxic and corrosive fluids. However, the efficiency of magnetic pumps is relatively low. Improving the efficiency of pumps helps to reduce energy loss and lower industrial costs. In this study, a magnetic pump was chosen as the research subject. The study aims to improve the efficiency and stability of the magnetic pump by optimizing the impeller blades based on the load curve. A combined approach of a numerical simulation and experimental verification was used to investigate the impact of the anterior loading point (AL), posterior loading point (PL), and slope (SL) in the blade loading curve on the pump's performance. The slope, which had the most significant impact on pump performance, was selected as the dependent variable to analyze the internal pressure pulsation and main shaft radial force of the magnetic pump. The research found that the hydraulic performance test results of the magnetic pump were in good agreement with the simulation results. When efficiency is used as the optimization objective, the anterior loading point should be moved as far back as possible, and the posterior loading point should be moved as far forward as possible. Through the study of internal pressure fluctuations and radial forces within the pump, the radial force distribution is sequentially as follows: the anterior loading method, posterior loading method, and middle loading method at a rated flow rate. The maximum pressure pulsation amplitude was near the volute casing diffuser area. Compared to the original pump, the optimized magnetic pump showed a 5.05% improvement in hydraulic efficiency under the rated conditions. This research contributes to enhancing the performance and efficiency of magnetic pumps, making them more suitable for various industrial applications.

Keywords: magnetic pump; optimization; load curve; pressure pulsation; radial force

MSC: 76U05

Citation: Zhang, R.; Wang, J.; Qian, W.; Geng, L. Optimization of Magnetic Pump Impeller Based on Blade Load Curve and Internal Flow Study. *Mathematics* **2024**, *12*, 607. https://doi.org/10.3390/math12040607

Academic Editor: Carlos Conceicao Antonio

Received: 12 December 2023
Revised: 9 January 2024
Accepted: 15 January 2024
Published: 18 February 2024

1. Introduction

In industries such as the chemical, biopharmaceutical, and petroleum ones, centrifugal pumps are commonly used to transport hazardous materials that are toxic and corrosive. However, traditional centrifugal pumps are designed with mechanical seals which creates a risk of leakage. Magnetic pumps achieve complete leak-free operation by using a magnetic drive to connect the prime mover and the working machine while isolating them with a containment shell [1]. This design replaces the dynamic seals found in traditional pumps with static seals [2].

As the core component of the magnetic pump, the design of the impeller blade directly affects the performance of the magnetic pump. The inverse problem design method of the impeller is to calculate the blade shape through reverse iteration given the blade load distribution, and only a few parameters need to be controlled to design the three-dimensional shape of the blade. The design cycle is short, and the dependence on experience

is low [3]. Blade load design is generally based on the inverse problem design of ternary theory, which is mostly used in the field of compressors. WU [4] first proposed the theory of three-dimensional flow, which has been widely applied in the design of turbomachinery internationally. Afterwards, with the development of CFD technology, the design of impellers became more convenient and efficient [5]. The shape design of load curves is diverse. Zhang and Zhao [6] selected a centrifugal pump for the proposed inverse methods to verify the reliability and accuracy of both inverse problem models, and research has found that inverse problem design methods can design more accurate centrifugal pump impeller models. Wang et al. [7] proposed a simple kinematic equation based on a reverse design for the secondary flow phenomenon in centrifugal pumps, which effectively controls the distribution of rotational gradients and suppresses the secondary flow, thereby expanding the efficient range of the pump, improving flow uniformity, and suppressing pressure fluctuations. Lu et al. [8] presented a modified inverse design method. In the new method, after a series of physical and mathematical simplifications, a sail-like constrained area is proposed, which can be used to configure different runner blade shapes. Through comparative analysis using the target runner blade, it was found that the maximum efficiency improvement reached 1.6%, while the head improvement was about 10%. Xu et al. [9] compared the hydraulic efficiency, flow field characteristics, pressure pulsation, etc., of two types of impellers by changing the blade load. The hydraulic characteristics and pressure pulsation were significantly affected by the blade load. The efficiency of the impeller increases with the increase in the load, and the pressure pulsation and radial force also increase. Zhu et al. [10] conducted the multi-objective optimization of centrifugal pump impellers using a three-dimensional inverse design method, taking the blade load, blade lean, and meridional channel shape as the optimization parameters, and research found that the runner with a negative blade lean has better stability than the runner with a positive blade lean.

Magnetic pumps belong to rotating machinery, and their internal flow is affected by the dynamic and static interference between the rotating impeller and the pump body [11]. This has a certain impact on the stable operation of the unit. For ordinary centrifugal pumps, the generation of pressure pulsation mainly comes from the vibration and noise caused by the blade sweeping over the pump body tongue, and the shape of the blade determines the speed and direction of the fluid flowing out of the impeller.

Therefore, the influence of impeller blade parameters on pressure pulsation cannot be ignored [12]. Many scholars have done a lot of research on this. Yang et al. [13] established a compressible model using the Tait equation to consider the impact of water compressibility on the numerical simulation process of hydraulic machinery. Through the combination of experimental and numerical simulation methods, it was found that the compressibility of water can affect the amplitude of pressure fluctuations at certain discrete frequencies, especially at the impeller outlet and volute tongue, where obvious jet wake and interactions between moving and stationary blades occur. Yang et al. [14] investigated the inter-stage difference of internal flow field distribution and the pressure pulsation characteristics inside a typical three-stage ESP. Then, a comparative analysis of the flow fields inside the impellers, diffusers, and chambers under different flow conditions was performed. The results show that the pressure pulsations caused by the interference phenomenon can seriously threaten the operational stability of ESP by inducing vibration and noise. Zhang et al. [15] used the Delayed Separation Eddy Simulation (DDES) method to study the transient flow and pressure pulsation of low-specific speed centrifugal pumps under stall conditions. This method can effectively capture the jet wake basin, and the volute structure has a significant impact on the evolution of the stall vortex structure. Cui et al. [16] presented the hub cutting of the impeller to suppress the rotor–stator interference between the blade and volute tongue in a high-speed centrifugal pump with double volutes. The flow fields in the centrifugal pumps with four hub-cutting angles were numerically simulated to investigate the influence on the internal flow and pressure pulsation. The results show what is under the design flow rate. The pressure pulsation intensity at the volute and the unsteady radial

force of the hub-cutting pumps are smaller than that of the prototype pump due to the flow improvement. In addition, the maximum and average values of the unsteady radial force decrease with the increase of the cutting angle.

According to the above literature analysis, many scholars have conducted extensive research on the optimization and internal flow mechanism of magnetic pumps, but have not analyzed the effects of the anterior loading point, posterior loading point, and slope on the performance of magnetic pumps based on blade load theory, or explored the laws of blade load curves. Therefore, this article mainly studies a magnetic pump. Based on the blade load curve, the impeller structure was optimized and analyzed to explore the influence of the impeller structure on the external characteristic energy of the pump. The influence of the internal pressure pulsation and axial radial force on the impeller before and after optimization was analyzed.

2. Numerical Simulation and Experiment

2.1. Theoretical Basis

In this research, various load distribution patterns are designed for cylindrical blades based on the blade load curve to explore various characteristic parameters in the blade load, namely the influences of the anterior loading point (AL), posterior loading point (PL), and slope (SL) on the pump's efficiency, head, internal flow, and other characteristics. The blade load curve is shown in Figure 1.

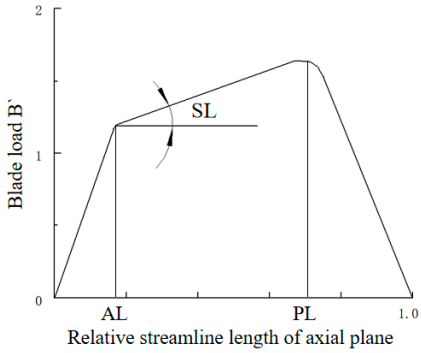

Figure 1. Distribution curve of blade load.

The blade load distribution is closely related to the velocity circulation and the relationship as follows:

$$p^+ - p^- = \frac{2\pi}{z}\rho\omega_m\frac{\partial(rV_\theta)}{\partial m} \tag{1}$$

In the above equation, p^+ represents the static pressure on the pressure surface of the blade and p^- donates the static pressure on the suction surface of the blade, both in Pa (pascals); z is the number of blades; ρ is the fluid density; ω_m is the relative velocity on the blade surface in m/s (meters per second); rV_θ represents the velocity circulation in m^2/s; and m is the relative length along the streamline blade (with a range of values from 0 to 1).

From the above equation, it can be seen that the pressure difference between the blade pressure surface and the suction surface is directly proportional to the $\frac{\partial(v_\theta r)}{\partial m}$, which is denoted as 'Blade Loading' for the convenience of the design:

$$B' = \frac{\partial(v_\theta r)}{\partial m} \tag{2}$$

The blade load curve is typically simplified to a three-segment curve, with three parameters defined to control the curve: the AL, PL, and SL. Based on the load curve,

the three-dimensional shape of the blade can be solved iteratively using the blade profile differential equation, as given by the equation:

$$df = \frac{\omega r^2 - rV_\theta}{V_m r^2} ds \tag{3}$$

where f represents the blade wrap angle; ω is the angular velocity of the impeller; r is the radius of the blade node; V_θ is the circumferential velocity at that node; V_m is the axial velocity component; and s represents the length along the axial streamline.

2.2. Physical Model and Computational Domain Model

A cylindrical vane magnetic pump with a specific speed of 92.7 r/min was selected as the research object; its main components consisted of the impeller, volute, back gap, front pump chamber, rear pump chamber circulation circuit, the inner hole of the impeller shaft, as well as inlet and outlet tubes, which are shown in Figure 2. The flow rate and head are the basic indicators for the application scenario of the magnetic pumps. On this basis, the spatial size of the pump's working environment affects our consideration of the parameters such as the speed and diameter, hence the main design parameters of the magnetic pump are shown in Table 1.

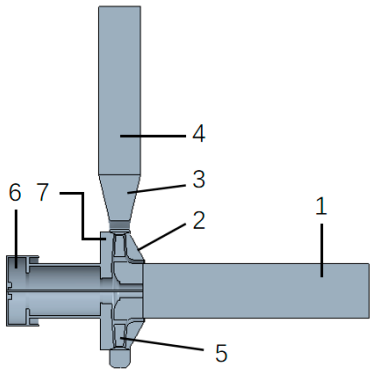

Figure 2. Pump full flow field water model. 1. Inlet tube; 2. Front pump chamber; 3. Volute; 4. Outlet tube; 5. Impeller; 6. Inner hole of impeller shaft; 7. Rear pump chamber circulation circuit.

Table 1. Main parameters of the magnetic pump.

Parameter	Symbol	Value	Unit
Design flow rate	Q	50	m^3/h
Design speed	n	2900	r/min
Head	H	32	m
Shaft power	P	7.5	kW
Inner diameter	D	85	mm
Number of impeller blades	$Z1$	6	/
Wrap angle	$Z2$	100	°

2.3. Grid Generation

The number of grids is a significant factor that affects the accuracy of the numerical simulation results. To verify the influence of the grid number on the numerical simulation results, six sets of grid numbers are selected to validate the influence of the mesh count on the numerical simulation results. The pump's head and efficiency values essentially stabilize when the total mesh count exceeds 2.5 million, as shown in Table 2. At this point, the impact of changes in the number of grids on the simulation results can be ignored. Therefore, a total mesh count of 2,484,601 is ultimately selected for the subsequent simulation calculations.

Table 2. Validation of grid independence.

Component	Grid 1	Grid 2	Grid 3	Grid 4	Grid 5	Grid 6
The number of grids	1,060,773	1,720,188	1,929,446	2,484,601	2,882,167	3,372,629
H(m)	35.88	35.94	35.98	36.09	36.12	36.14
η(%)	74.64	74.39	74.42	74.5	74.48	74.49

Structured grids are used for all fluid domain models for their excellent adaptability to flow domain models with variations in length and width, especially for small domains like gap clearances. The global grid quality exceeds 0.2. The total computational fluid domain for the numerical simulation contains six parts: the impeller, volute, back gap, and inlet and outlet tubes. Figure 3 shows the computational domains and mesh details.

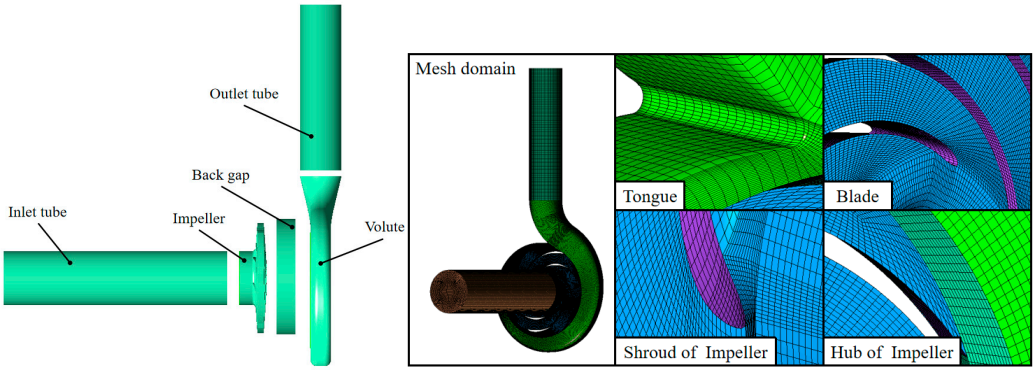

Figure 3. Flow domain and mesh details.

3. Research Methods

3.1. Numerical Simulation

The numerical simulation for the magnetic pump was conducted by the ANSYS CFX. The SST *k-w* turbulence model was chosen which can simulate the flow phenomenon near the wall surface better. The liquid phase was water at 25 °C during the research object. The impeller flow region and the impeller shaft inner bore region were part of the rotating domain, while other regions such as the front and rear pump chambers, volute region, and inlet and outlet section were parts of the stationary domain in the entire pump flow field. Static stationary interfaces and dynamic stationary interfaces are defined based on the states of these domains, respectively. The inlet and outlet boundary conditions were set to the pressure and flow rate for solving, respectively. This article maintains the inlet pressure and pump speed as fixed values, and achieves numerical simulation of different working conditions by changing the value of the outlet flow rate.

3.2. Experimental Verification

The experimental and numerical simulations for the original model were carried out based on the settings mentioned above to measure the head and efficiency of the magnetic pump. The experimental equipment was adjusted to the measured operating condition and kept running for 30 min, then the output signal was collected for 10 s and averaged, and the results were analyzed using a computer data acquisition and processing system to plot performance curves. The hardware system employed NI's PXI system and a multifunction dynamic data acquisition card, while the software system utilized NI's LabVIEW suite for collecting various performance parameters of the pump. The sensors involved in the experiment include flow meters, pressure sensors, and torque meters. The data collected in the experiment were analyzed using uncertainty standards and the measurement range of the pressure gauge was −0.1~1.5 MPa, with an allowable error of ±0.0256 MPa. The measurement range of the flow meter was 10–100 m^3/h and its allowable error was ±1.5 m^3/h. The measurement range of the torque meter was 0–200 nm and its allowable error was ±1 nm. The uncertainty analysis formula is shown below [17].

This article collected signals continuously for 10 s under stable experimental conditions and calculated the average based on the number of times collected. Figures 4 and 5 illustrate the schematic diagram of the test system and the test platform.

$$y = f(x_1, x_2, \cdots, x_N) \tag{4}$$

$$y = \overline{Y} = \frac{1}{n}\sum_{k=1}^{n} f(x_{1,k}, x_{2,k}, \cdots, x_{N,k}) \tag{5}$$

Figure 4. Testing system of carbon fiber composite magnetic pump.

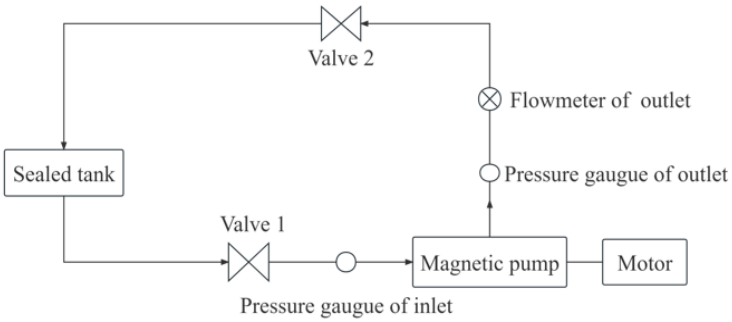

Figure 5. Schematic diagram of the test platform.

Figure 6 shows the experimental external characteristic curves and numerical simulation values for the magnetic pump at various flow points under a rated speed. At the rated flow rate (Q_d), the relative error between the experiment (34.23 m) and numerical simulation (33.31 m) values for head was 2.7%.

The results indicate that the numerical simulation can only estimate the hydraulic loss, mechanical loss, and volume loss, which inevitably leads to errors, and the simulation values are often higher than the experimental values. So the simulation results exhibit a good agreement with the experimental results and the optimization was based on this impeller.

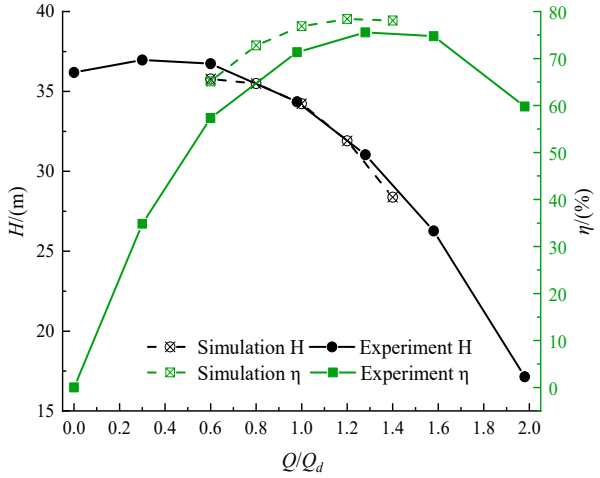

Figure 6. Characteristic curve of pump experiment.

Due to the fact that the numerical simulation only calculates the hydraulic efficiency of the entire flow field of the pump, while the efficiency of the magnetic pump unit is obtained by multiplying through sets of efficiency; the formula is as follows:

$$\eta_{unit} = \eta_{pump} \cdot \eta_{motor} \tag{6}$$

$$\eta_{pump} = \eta_{hydraulic} \cdot \eta_{transmission} \cdot \eta_{machinery} \tag{7}$$

At the rated flow point, the Unit efficiency (η_{unit}) is 65.15% and pump efficiency (η_{pump}) is 71.36%. According to Equation (6), the motor efficiency (η_{motor}) can be obtained as 91.3%. This is consistent with the efficiency of the motor with a power of 11 kW and model YE2-160M1-2P. The pump mechanical efficiency ($\eta_{machinery}$) is 95%, and the magnetic transmission efficiency of the magnetic pump is 95%.

According to the experimental values, it can be seen that under the rated flow rate, the efficiency of the pump unit obtained from the experiment is 65.15%, while the hydraulic efficiency calculated from the simulation is 76.87%. According to the above formula, the efficiency of the simulated pump unit can be calculated as:

$$\begin{aligned} \eta_{simulation} &= 76.87\% \times 95\% \times \\ &95\% \times 91.3\% = 63.27\% \end{aligned} \tag{8}$$

The efficiency error value is around 2.9%, which is consistent with the efficiency of the test unit. According to the comparison of the head and efficiency values, the simulation calculation results are reliable.

3.3. Optimal Design of Impeller

This study focuses on a cylindrical blade magnetic pump with a specific speed of 92.7. The research considers different loading schemes for the impeller. The range for the anterior loading point is (0.2, 0.5), the range for the posterior loading point is (0.5, 0.8), and the slope is varied among −0.5, −1, 0, 1, and 2. The experimental design first selected different AL schemes (Scheme 1, 2, 14, 15, 18, and 19) with a PL of 0.6 and SL of 1 and 2. It was found that the efficiency of the front loading point was at a higher value when it was moved back, and the efficiency peak was at an AL of 0.4. Under these conditions, data with different PL or SL values were calculated for single factor analysis, and the following 19 schemes were generated according to this method, while the remaining components of the pump were kept unchanged. The numerical simulations were conducted to obtain the simulated head and efficiency for each loading scheme, as presented in Table 3. To determine how each characteristic parameter of the load curve affects the pump's external characteristics and to accurately understand the variations in the pump's external characteristics under different

loading schemes, this study investigates the impact of these three characteristic parameters on the internal flow and hydraulic performance of the pump.

Table 3. Simulation value of impeller efficiency of part of scheme.

	AL	PL	SL	$1.0Q{\cdot}\eta$(%)	$1.0Q{\cdot}H$/(m)
1	0.2	0.6	1	78.79	32.95
2	0.2	0.6	2	78.87	32.93
3	0.2	0.8	−1	77.27	34.73
4	0.2	0.8	−0.5	77.72	35.27
5	0.2	0.8	0	78.88	32.52
6	0.2	0.8	1	79.47	32.61
7	0.3	0.7	1	79.37	32.89
8	0.3	0.7	2	79.51	32.66
9	0.4	0.5	−1	78.56	34.1
10	0.4	0.5	0	78.8	33.15
11	0.4	0.5	2	79.6	33.58
12	0.4	0.6	−1	78.0	35.55
13	0.4	0.6	0	79.02	32.95
14	0.4	0.6	1	79.23	32.96
15	0.4	0.6	2	79.53	33.12
16	0.4	0.7	1	79.42	32.95
17	0.4	0.7	2	79.36	32.93
18	0.5	0.6	1	78.64	34.73
19	0.5	0.6	2	78.59	35.27

To explore the effects of the AL, PL, and SL on the performance of magnetic pumps, a scheme with a different value and the two same values was selected for analysis. Figure 7 shows the distribution of the blade load curves at different anterior loading points, impellers 2, 15, and 19 were selected for analysis, whose ALs were 0.2, 0.4, and 0.5, and the PL and SL were 0.6 and 2, respectively. It can be observed that changes in the anterior loading point have a significant impact on the front part of the blade, while the differences in the load curve for the rear part of the blade are relatively small. Figure 8 displays the numerical simulation results for impeller 2, impeller 15, and impeller 19 at different flow points. At $0.6Q_d$, the variations in efficiency and head values are relatively small for all schemes. In the range of $0.8Q_d$ to $1.0Q_d$, the highest efficiency values in the sequence are impeller 15, impeller 2, and impeller 19, and the highest head values in the sequence are impeller 19, impeller 15, and impeller 2. At high flow rates, impeller 15 experiences the greatest decrease in efficiency, and impeller 2 has the highest efficiency, while impeller 19 achieves the maximum head value. Since the pumps typically operate near the rated conditions, the study focuses on the variations in the range of $0.8Q_d$ to $1.2Q_d$. When the anterior loading point is moved backward, the efficiency increases. However, when the anterior loading point is at 0.5, there is a sudden drop in efficiency, and impeller 19 achieves the maximum head value. Therefore, it is recommended to keep the anterior loading point as close to 0.4 as possible and move it backward during the design process.

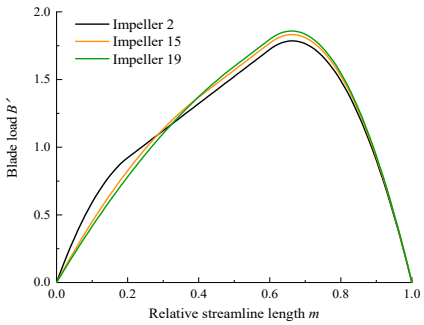

Figure 7. Blade load curve scheme under different anterior loading points.

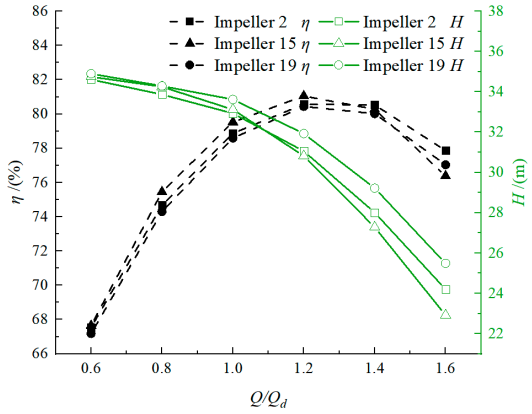

Figure 8. Performance curves of pumps with different anterior loading points.

To analyze the impact of the posterior loading points on the external characteristics of the pump, the posterior loading points were taken as 0.5, 0.6, and 0.7, respectively. The anterior loading points remained unchanged at 0.4, with slopes of 2 for impellers 11, 15, and 17. Figure 9 displays the blade load curve schemes at different posterior loading points.

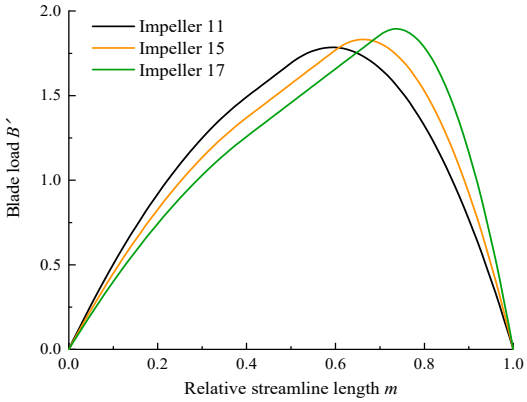

Figure 9. Scheme of blade load curve under different posterior loading points.

Figure 10 shows the external characteristic curves for impellers 11, 15, and 17 obtained from numerical simulations. Based on the curves in the figure, it can be observed that the influence of the posterior loading point on the pump's external characteristics exhibits greater fluctuations compared to the anterior loading point. In the range of $0.6Q_d$ to $0.8Q_d$, when the posterior loading point is moved backward, there is a slight increase in efficiency. However, within the flow range of $1.0Q_d$ to $1.2Q_d$, the highest efficiency values in the sequence are for impellers 11, 17, and 15, and the head values are in the order of impellers 11, 15, and 17. The posterior loading point has a greater impact on the head values than the anterior loading point and has a relatively smaller effect on the efficiency values. To strike a balance between the head and efficiency values, it is recommended to set the posterior loading point at 0.5.

According to the simulation calculation results in the previous section, the influence of the slope on the pump performance is greater than that of the anterior and posterior loading points. Therefore, the slope is chosen as the subject of an in-depth analysis of the internal flow within impellers 3, 4, 5, and 6. In these cases, the anterior and posterior loading points are both set at 0.2 and 0.8, while the slopes are set to -1, -0.5, 0, and 1, respectively. The distribution of the load curve is shown in Figure 11, where the SL is less than 0 and the maximum load distribution is located near the leading edge of the relative streamline of the blade, which is called anterior loading. Similarly, when the SL is greater than 0, it is called posterior loading; when the SL is equal to 0, it is called middle loading.

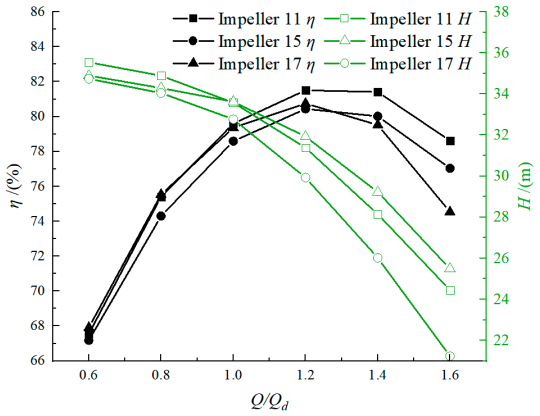

Figure 10. Performance curves of pumps with different posterior loading points.

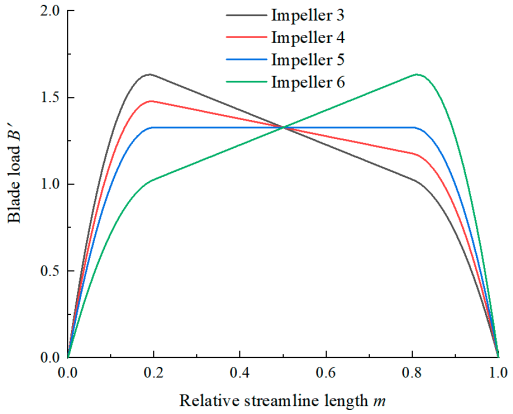

Figure 11. Blade loading curve scheme under different slopes.

Tables 4 and 5, respectively, show the impacts of the load curve with different SLs on the efficiency and head of the pump under different operating conditions. When the SL is less than 0, the pump efficiency is significantly lower, while the head is higher. With an increase in the slope, both the efficiency and head values improve across various operating conditions. When the SL is equal to 0, there is a noticeable increase in efficiency and a significant decrease in the head values. When the SL is greater than 0, as the slope increases, the high-efficiency region shifts forward. When operating near $1.0Q_d$, both the efficiency and head values increase. The sign of the slope (positive or negative) plays a decisive role in the impeller efficiency. According to the blade profile equation, the larger the circulation, the smaller the blade wrap angle. When the SL is a positive value, the blade wrap angle is larger, and when the SL is a negative value, the blade wrap angle is smaller. If the blade wrap angle is too large, it can result in the elongation of the impeller flow path and increased losses along the path which leads to a reduction in the pump efficiency and head. Therefore, it is advisable to select an appropriate slope value for the load curve during the design phase.

Table 4. Simulation value of impeller efficiency of each scheme.

	AL	PL	SL	0.6*Q*/(%)	0.8*Q*/(%)	1.0*Q*/(%)	1.2*Q*/(%)	1.4*Q*/(%)	1.6*Q*(%)
3	0.2	0.8	−1	65.15	72.63	77.27	79.49	79.03	76.33
4	0.2	0.8	−0.5	65.05	73.08	77.72	80.06	80.2	78.65
5	0.2	0.8	0	67.69	74.83	78.88	80.73	80.57	77.86
6	0.2	0.8	1	67.78	75.28	79.47	81.24	80.42	76.92

Table 5. Simulation value of impeller head for each scheme.

	AL	PL	SL	0.6Q/(%)	0.8Q/(%)	1.0Q(%)	1.2Q/(%)	1.4Q/(%)	1.6Q(%)
3	0.2	0.8	−1	36.47	36.33	34.73	32.6	28.87	24.98
4	0.2	0.8	−0.5	37.15	36.93	35.27	33.646	30.24	26.85
5	0.2	0.8	0	34.37	33.66	32.52	30.56	27.6	23.84
6	0.2	0.8	1	34.47	33.88	32.61	30.39	26.78	22.47

Through steady calculations, the external characteristic curves for the four impellers of the magnetic pump are obtained at different flow conditions, as shown in Figure 12. Impeller 4 exhibits the highest head curve values at full flow conditions, followed by impeller 3, and impeller 6 has nearly identical head values at low flow rates with impeller 5, which shows a noticeable decrease in head values at high flow rates. In terms of efficiency, impeller 6 achieves the highest efficiency near the rated flow rate (0.8Q_d to 1.2Q_d), with a significant decrease in efficiency in off-design conditions. Impeller 5 follows, with efficiency trends that are generally consistent with impeller 6. Impeller 4 has lower efficiency values at low flow rates, and efficiency decreases more slowly at high flow rates. When the flow rate exceeds 1.4Q_d, impeller 4 gradually surpasses the three other impellers in efficiency. However, impeller 3 consistently exhibits the lowest efficiency values across all flow conditions.

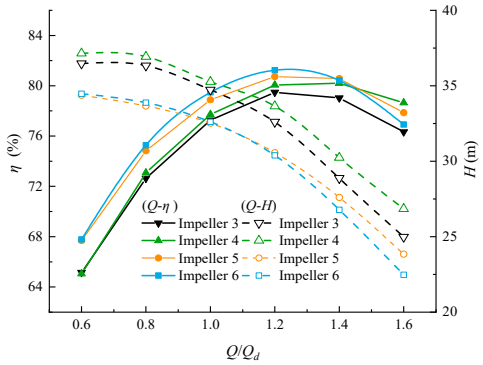

Figure 12. Performance curves of pumps under different slopes.

3.4. Comparative Analysis of Optimization Results

Based on the above rules, impeller 11, with an anterior loading point (AL) of 0.4, a posterior loading point (PL) of 0.5, and a slope (SL) of 2, was initially selected as the optimized impeller, as shown in Figure 13. Impeller 11 consistently exhibited significantly higher hydraulic efficiency under all working conditions compared to the original impeller. The most significant improvement in efficiency is observed at the rated operating condition, with an increase of 5.05%. While the optimized impeller experiences a slight reduction in head, it remains within the design specifications.

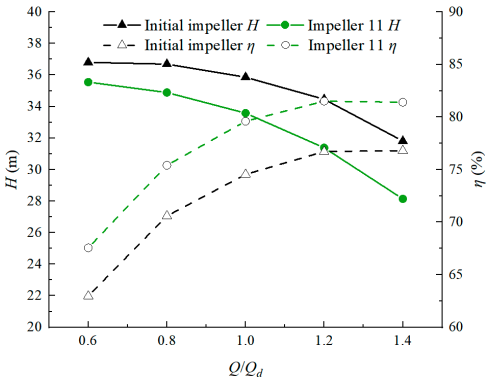

Figure 13. Performance curves of the original impeller and optimized impeller.

4. Analysis of Unsteady Internal Flow in Impeller Based on Blade Load Curve

During the operation of the pump, vibrations caused by the interaction between the impeller and the volute affect the strength of the impeller to some extent. As analyzed in the previous sections, the slope of the blade loading curve has a significant impact on the pump's external performance. However, it is not known whether the internal pressure pulsation characteristics of the pump are affected. Therefore, impellers 3, 5, and 6 with different slope values of the loading curve (−1, 0, 1) are selected for unsteady numerical calculations to investigate the patterns of pressure pulsation and radial force. Based on this, a comparative analysis of non-steady internal flow is conducted between the optimized impeller and the original pump impeller.

To study the patterns of pressure pulsation inside the magnetic pump's dynamic and static rotor components, monitoring points are identified at various locations. Specifically, two points are taken on the pressure surface and suction surface of the impeller blades separately and denoted as P1 and P4, respectively. A monitoring point, P2, is defined in the second cross-section of the volute, and another monitoring point, P3, is set at the tongue. This setup is illustrated in Figure 14.

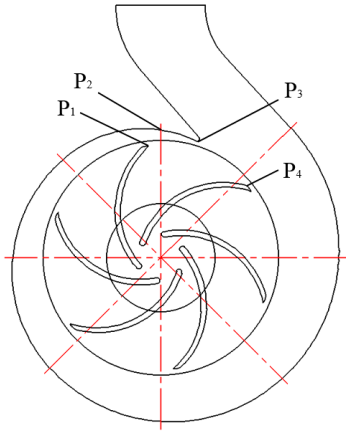

Figure 14. Distribution diagram of monitoring points in pump.

Due to significant differences in pressure levels at various monitoring points within the flow domain, the dimensionless coefficient C_p which is defined as the pressure pulsation coefficient is introduced to facilitate the measurement of the pulsation levels, and its formula is as follows:

$$C_p = \frac{p - \overline{p}}{0.5\rho u_2^2} \tag{9}$$

where p is the static pressure value at that location, in Pa; $\overline{p}$ is the average static pressure value during that period, in Pa; ρ is the fluid density, in kg/m^3; and u_2^2 is the circumferential velocity value at the outlet of the impeller, in m/s.

$$u_2 = \frac{\pi D_2 n}{60} \tag{10}$$

where D_2 is the impeller outer diameter, in meters, and n is the impeller rotational speed, in r/min.

The volute generates a certain radial force during the operation of the pump. If the radial force acting on the impeller is too large, it may affect the stable operation and lifespan of the pump. Therefore, it is necessary to analyze the radial forces on the impeller.

The radial forces on the blade surface can be divided into horizontal and vertical components. In CFD numerical simulation software, the impeller rotates around the Y-axis. Therefore, the horizontal and vertical components of the forces F_x and F_z are extracted from

the blade surface in the X and Z directions, respectively. The radial force is then calculated using the formula for the resultant radial force:

$$F = \sqrt{F_x^2 + F_z^2} \tag{11}$$

where F_x is the resultant radial force on the blade surface in the X-axis direction, and F_z is the resultant force on the blade surface in the Z-axis direction.

4.1. Comparative Analysis of Pressure Pulsation

Based on the analysis of the pressure pulsation inside the pump in Figure 14, it can be observed that the maximum amplitude of pressure pulsation mainly occurs at the impeller outlet, near the diffuser, and at the second cross-section of the volute casing. Therefore, monitoring points P1, P2, P3, and P4 are selected for the analysis of non-steady pressure pulsation under various operating conditions ($0.8Q_d$, $1.0Q_d$, and $1.2Q_d$) for both the original pump and impeller 11.

Figure 15 illustrates the variation in the pulsation amplitude at these four monitoring points for different flow rates. Monitoring points P1 and P2 are located at the back and front surfaces of the impeller outlet. For the original pump, the pulsation variations are stronger across all three flow rates compared to impeller 11. As the flow rate increases, the pulsation amplitude decreases, and the pulsations become smoother. When the pump operates at low flow rates, the flow velocity inside the impeller decreases, which leads to an unsteady flow, an increase in pressure, and the rise in the pulsation amplitude.

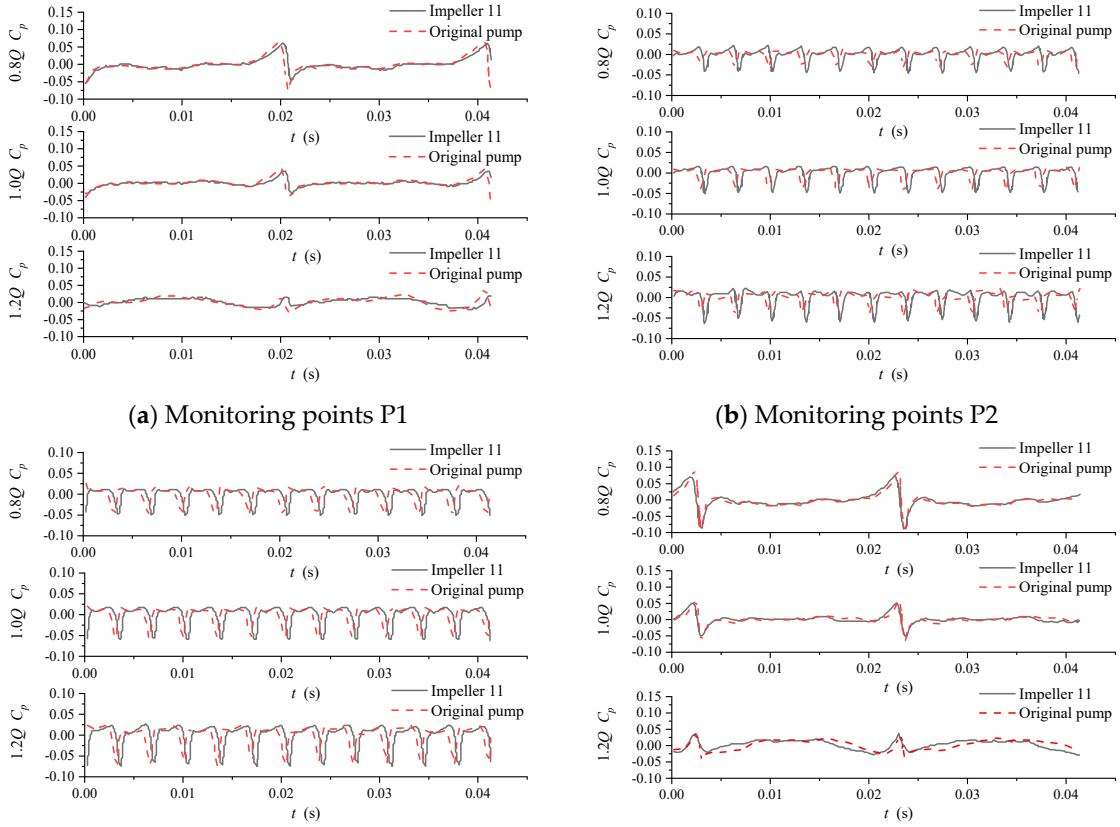

(**a**) Monitoring points P1

(**b**) Monitoring points P2

(**c**) Monitoring points P3

(**d**) Monitoring points P4

Figure 15. Time domain diagram of pressure pulsation in pumps.

At monitoring points P2 and P3, the amplitude of impeller 11 under various operating conditions is slightly higher than that of the original pump, which is contrary to the pulsation pattern in the impeller basin. Impeller 11 has a lower head compared to the

original pump, resulting in higher flow velocities exiting the impeller. The fluid impacts the diffuser at a high speed which leads to pulsations. Most of this flow is directed toward the outlet of the volute, with a smaller portion entering the interior of the volute and subsequently flowing out.

Further analysis based on the frequency domain plots of pulsations for the original pump and impeller 11 reveals some interesting findings, as shown in Figure 16. At monitoring point P1, the original pump exhibits higher pulsation amplitudes compared to impeller 11, while at monitoring point P4, the pulsation amplitudes are lower for impeller 11. At low flow rates, the impeller is significantly affected by shaft frequency harmonics. Beyond one times the shaft frequency, the pulsation amplitudes gradually decrease, and impeller 11 consistently exhibits lower pulsation amplitudes compared to the original pump's impeller. As the flow rate increases, the amplitudes of shaft frequency harmonics decrease, and the primary frequency of pressure pulsation becomes one times the shaft frequency. Analyzing the pulsation curves from monitoring points P1 and P4 within the impeller flow domain reveals that the lowest pulsation amplitudes are observed at the rated flow rate, while at off-design flow rates, the pulsation peaks are generally larger.

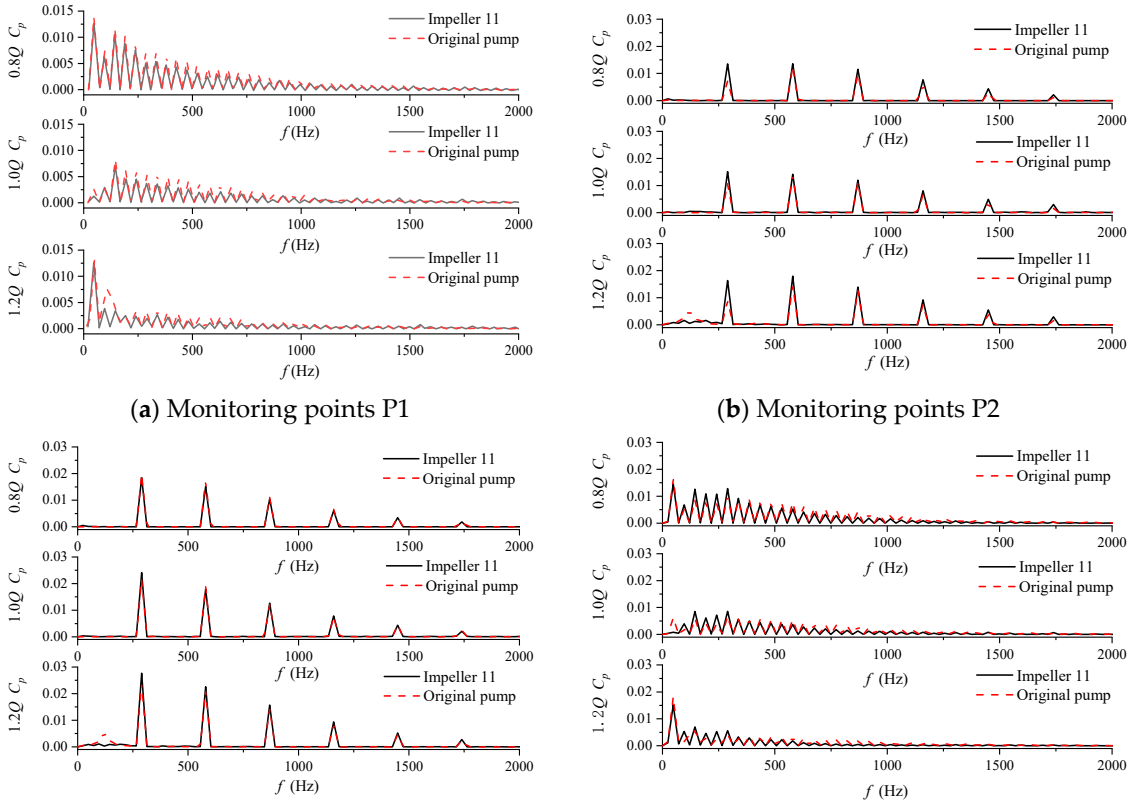

(**a**) Monitoring points P1 (**b**) Monitoring points P2

(**c**) Monitoring points P3 (**d**) Monitoring points P4

Figure 16. Frequency domain diagram of pressure pulsation in pumps.

In the volute flow domain, monitoring points P2 and P3 exhibit primary frequencies corresponding to the blade passing frequency. The pulse of monitoring point P3 at the tongue is mainly caused by impact, which is related to the operating flow. At $0.8Q_d$, the pulsation peak at P3 for impeller 11 is approximately 2.1 times that of the original pump's impeller, while it is approximately 1.5 times that of the original pump at the rated flow rate. The pulsation amplitudes at monitoring point P2 increase with the increase in the flow rates, as the increase in the flow velocity at the impeller outlet and the area of the volute section at this point is smaller, which results in a higher pressure distribution. Comparing the pulsation amplitudes at monitoring points P2 and P3 under various operating conditions, it can be observed that P3 consistently has the highest amplitudes. This is because the tongue

is influenced by both the dynamic and static interference from the impeller and the impact of the fluid expelled by the impeller.

4.2. Comparative Analysis of Radial Force Distribution

Figure 17 shows the radial force distribution of the original pump impeller and impeller 11 at three different flow rates. Both exhibit the smallest radial force distribution at the rated flow rate. The maximum radial force component is 11.9 N for the original pump and 11.72 N for impeller 11 at the rated flow rate. In theory, the design of the volute section should ensure that the fluid velocity and pressure inside the volute are evenly and axially symmetrically distributed, only at the rated flow rate. When the pump operates at off-design conditions, the radial forces on the impeller increase significantly. At $0.8Q_d$, the maximum radial force components for the original pump and impeller 11 are 62.64 N and 54.83 N, respectively, which are approximately six times higher than the rated flow rate. At $1.2Q_d$, the maximum radial force components for the original pump and impeller 11 are 56.88 N and 62.21 N, respectively. Changes in the velocity and direction of the fluid happen inside the volute and at the outlet of the impeller, resulting in impacts and increased pressure in the diffuser section. This disruption of axial symmetry in the volute casing flow domain leads to a significant increase in radial forces. Impeller 11 exhibits a substantial increase in radial forces at high flow rates, which is related to the design flaw in the blade loading. The impeller designed with blade loading has a narrow high-efficiency region, causing a significant drop in performance at high flow rates. It is recommended to operate impellers designed with blade loading at the rated flow rate and low flow rates.

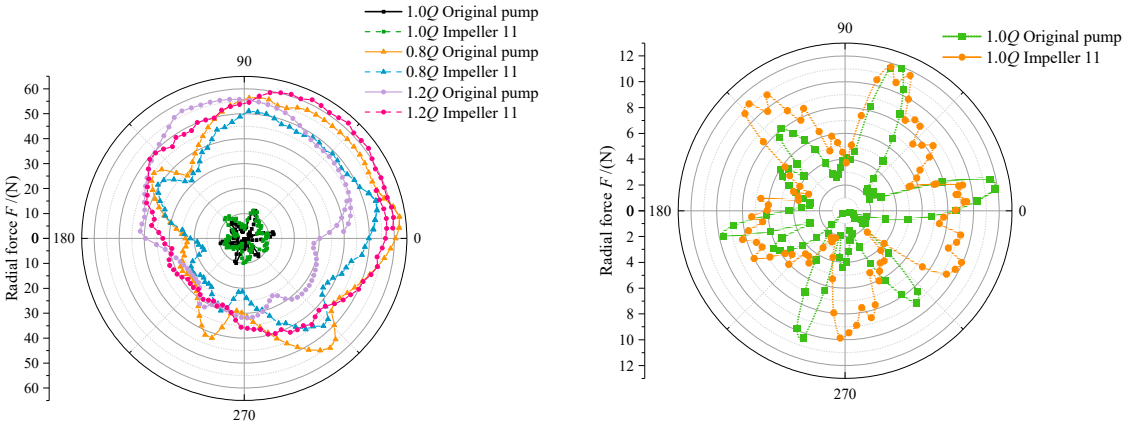

(**a**) Comparison of radial forces under different operating conditions

(**b**) Comparison of radial forces under rated operating conditions

Figure 17. Vector diagram of radial force.

5. Conclusions

(1) This article is based on the blade load theory to reverse design the magnetic pump, providing a new method to increase the efficiency of the magnetic pump and reduce energy loss in production. The specific conclusion is as follows: If efficiency is chosen as the optimization objective, the anterior loading point should be moved as far back as possible, while the posterior loading point should be moved as far forward as possible, but the value of m should not exceed 0.5. The SL of the loading curve has the most significant impact on pump performance. When the SL is less than 0, the efficiency of the magnetic pump is the lowest, and the head is the highest. As the SL increases, both the head and efficiency curves of the pump increase. But an excessive SL can lead to an excessive blade wrap angle which forms axial vortices, leading to a decrease in efficiency.

(2) In the impeller flow domain, the pulsation is mainly influenced by the shaft frequency and its harmonics. The pulsation magnitude on the suction surface of the blade is generally much smaller than on the pressure surface, and the pulsation magnitude

increases significantly with the radius of the blade. The maximum pulsation magnitude in the impeller flow domain is near the exit of the blade working surface. In the volute casing flow domain, the pulsation is mainly at the blade-pass frequency. With an increase in the volute casing section, the pulsation magnitude gradually decreases until it increases again at the diffuser section. Therefore, when designing a cylindrical impeller, a rear-loading approach should be adopted, meaning the blade loading curve slope should be greater than 0.

(3) At low flow rates, the impeller is significantly affected by the shaft frequency and its harmonics. Beyond one times the shaft frequency, the pressure pulsation amplitude slowly decreases. As the flow rate increases, the influence of the shaft frequency harmonics on the pulsation amplitude weakens, and it is mainly affected by the fundamental frequency. The magnitude of the radial force is directly proportional to the flow rate. Therefore, impellers optimized for blade loading should avoid operating at high flow rates.

Author Contributions: Conceptualization, R.Z. and W.Q.; methodology, J.W.; software, L.G.; validation, R.Z.; formal analysis, R.Z.; investigation, J.W.; resources, J.W.; data curation, J.W.; writing—original draft preparation, R.Z. and W.Q.; writing—review and editing, R.Z. and W.Q.; visualization, L.G.; supervision, J.W.; project administration, J.W.; funding acquisition, J.W. All authors have read and agreed to the published version of the manuscript.

Funding: Provincial Key Research and Development Program (BE2018085). Wenling Research Institute of Fluid Machinery, Jiangsu University independent project.

Data Availability Statement: The data in this study are available from the corresponding author upon request.

Acknowledgments: Wenling Fluid Machinery Technology Institute, Jiangsu University.

Conflicts of Interest: No potential conflicts of interest were reported by the author(s).

References

1. Brodersen, S. Magnetic-drive pumps: Technology and new applications. *Hydrocarb. Process.* **2001**, *80*, 45–48.
2. Thompson, K. What the future holds for magnetic drive pumps. *World Pumps* **2007**, *2007*, 28–29. [CrossRef]
3. Zhang, L.; Davila, G.; Zangeneh, M. Multi-objective optimization of a high specific speed centrifugal volute pump using three-dimensional inverse design coupled with computational fluid dynamics simulations. *J. Fluids Eng.* **2021**, *143*, 021202. [CrossRef]
4. Wu, C.H. A general theory of three-dimensional flow in subsonic and supersonic turbomachines of axial, radial, and mixed-flow types. *Trans. Am. Soc. Mech. Eng.* **1952**, *74*, 1363–1380. [CrossRef]
5. Zangeneh, M. Inviscid-viscous interaction method for three-dimensional inverse design of centrifugal impellers. *J. Turbomach.* **1994**, *116*, 280–290. [CrossRef]
6. Zhang, R.; Zhao, X. Inverse method of centrifugal pump blade based on Gaussian process regression. *Math. Probl. Eng.* **2020**, *2020*, 4605625. [CrossRef]
7. Wang, C.Y.; Wang, F.J.; An, D.S.; Yao, Z.; Xiao, R.; Lu, L.; He, C.; Zou, Z. A general alternate loading technique and its applications in the inverse designs of centrifugal and mixed-flow pump impellers. *Sci. China Technol. Sci.* **2021**, *64*, 898–918. [CrossRef]
8. Lu, Y.M.; Wang, X.F.; Wang, W.; Zhou, F.M. Application of the modified inverse design method in the optimization of the runner blade of a mixed-flow pump. *Chin. J. Mech. Eng.* **2018**, *31*, 105. [CrossRef]
9. Xu, Y.; Yang, A.L.; Lang, D.P.; Dai, R. Blade design loads on the flow exciting force in centrifugal pump. In Proceedings of the 26th IAHR Symposium on Hydraulic Machinery and Systems, Beijing, China, 19–23 August 2012. PTS 1-7.2013.
10. Zhu, B.; Wang, X.; Tan, L.; Zhou, D.; Zhao, Y.; Cao, S. Optimization design of a reversible pump–turbine runner with high efficiency and stability. *Renew. Energy* **2015**, *81*, 366–376. [CrossRef]
11. Perez, R.X.; Akins, R.A.; Lee, C.E.; Taylor, H.F. Fiber-optic pressure sensors detect cavitation and flow instabilities in centrifugal pumps. *World Pumps* **1996**, *1996*, 28–33. [CrossRef]
12. Wang, K.; Zhang, Z.; Xia, C.; Liu, Z. Experimental investigation of pressure fluctuation, vibration, and noise in a multistage pump. *Shock and vibration* **2018**, *2018*, 2784079. [CrossRef]
13. Yang, J.; Liu, J.; Liu, X.; Xie, T. Numerical study of pressure pulsation of centrifugal pumps with the compressible mode. *J. Therm. Sci.* **2019**, *28*, 106–114. [CrossRef]
14. Yang, Y.; Zhou, L.; Shi, W.; He, Z.; Han, Y.; Xiao, Y. Interstage difference of pressure pulsation in a three-stage electrical submersible pump. *J. Pet. Sci. Eng.* **2021**, *196*, 107653. [CrossRef]
15. Zhang, N.; Jiang, J.; Gao, B.; Liu, X. DDES analysis of unsteady flow evolution and pressure pulsation at off-design condition of a centrifugal pump. *Renew. Energy* **2020**, *153*, 193–204. [CrossRef]

16. Cui, B.; Liu, J.X.; Zhai, L.; Han, A. Analysis of the performance and pressure pulsation in a high-speed centrifugal pump with different hub-cutting angles. *Mod. Phys. Lett. B* **2023**, *37*, 2350117. [CrossRef]
17. BIPM. *Évaluation des Données de Mesur—Guide Pour l'Expression del'Incertitude de Mesure*; JCGM 100:2008; BIPM: Paris, France, 2008.